Channel Specific Rate Constants Relevant to the Thermal Decomposition of Disilane

Keiji Matsumoto,*,† Stephen J. Klippenstein,‡ Kenichi Tonokura,§ and Mitsuo Koshi†

Department of Chemical System Engineering, The University of Tokyo, 7-3-1 Hongo, Bunkyo-ku, Tokyo 113-8656, Japan, Combustion Research Facility, Sandia National Laboratories, Livermore, California 94551-0969, and Environmental Science Center, The University of Tokyo, 7-3-1 Hongo, Bunkyo-ku, Tokyo 113-0033, Japan

Received: December 25, 2004; In Final Form: March 3, 2005

Rate constants for the thermal dissociation of Si_2H_6 are predicted with a novel transition state model. The saddle points for dissociation on the Si_2H_6 potential energy surface are lower in energy than the corresponding separated products, as confirmed by high level ab initio quantum mechanical calculations. Thus, the dissociations of Si_2H_6 to produce $SiH_2 + SiH_4$ (R1) and $H_3SiSiH + H_2$ (R2) both proceed through tight inner transition states followed by loose outer transition states. The present "dual" transition state model couples variational phase space theory treatments of the outer transition states with ab initio based fixed harmonic vibrator treatments of the inner transition states to obtain effective numbers of states for the two transition states acting in series. It is found that, at least near room temperature, such a dual transition state model is generally required for the proper description of each of the dissociations. Only at quite high temperatures, i.e., above 2000 K for (R1) and 600 K for (R2), does a single fixed inner transition state provide an adequate description. Similarly, only at quite low temperatures (below 100 and 10 K for (R1) and (R2), respectively) does a single outer transition state provide an adequate description. Pressure dependent rate constants are obtained from solutions to the multichannel master equation. These calculations confirm that dissociation channel (R2) is negligible under conditions relevant to the thermal chemical vapor deposition (CVD) processes. Rate constants for the chemical activation reactions, $SiH_2 + SiH_4 \rightarrow Si_2H_6$ (R-1) and $SiH_2 + SiH_4 \rightarrow H_3SiSiH + H_2$ (R3), are also evaluated within the dual transition state model. It is found that reaction R3 is the dominant channel for low pressures and high temperatures, i.e., below 100 Torr for temperatures above 1100 K.

1. Introduction

Silane and disilane are routinely used as the source gases for silicon chemical vapor deposition (CVD) processes. Numerous researchers have studied the kinetics of their reactions as part of their efforts at modeling silicon CVD processes.[1−6] As a result, the gas-phase chemical kinetic mechanism is by now quite well established. There are, however, some important unresolved issues. In particular, some aspects of the thermal decomposition of Si_2H_6 and its reverse reactions have not yet been understood. The relevant elementary reactions are as follows:

$$Si_2H_6 \rightarrow SiH_2 + SiH_4 \quad \text{(R1)}$$

$$Si_2H_6 \rightarrow H_3SiSiH + H_2 \quad \text{(R2)}$$

$$SiH_2 + SiH_4 \rightarrow Si_2H_6 \quad \text{(R-1)}$$

$$SiH_2 + SiH_4 \rightarrow H_3SiSiH + H_2 \quad \text{(R3)}$$

$$H_3SiSiH + H_2 \rightarrow Si_2H_6 \quad \text{(R-2)}$$

$$H_3SiSiH + H_2 \rightarrow SiH_2 + SiH_4 \quad \text{(R-3)}$$

Three reactions (Si_2H_6 decomposition, $SiH_2 + SiH_4$, and $H_3SiSiH + H_2$) are listed above, and each reaction has two product channels. The greatest uncertainty in the implementation of models for these reactions involves the estimation of the branching ratios for each reaction pair. Rate constants for thermal decomposition of Si_2H_6 have been measured in static reactors[7−11] and in shock tubes.[12,13] However, experimental information on the rate constant for reaction R2 is very limited. For the reaction of SiH_2 with SiH_4, the rate constant for the overall decay of SiH_2 has been measured by several researchers.[18−26] However, no direct experimental information is available for (R3), with only one estimated value available from the shock tube experiment of Mick et al.[13] There does not appear to be any experimental information available for reactions R-2 and R-3.

Branching ratios for these three reaction pairs are essential for the understanding of the thermal silicon CVD processes and the primary purpose of the present study is to clarify the branching fractions of these reactions. Several researchers have performed RRKM calculations for the thermal decomposition of Si_2H_6.[14−21] According to these calculations, reaction R1 dominates, with reaction R2 being only a minor channel due to its higher heat of reaction. However, there are several limitations in these calculations.

The energy profile along the reaction coordinate for the reaction of $SiH_2 + SiH_4$ is complicated as shown by Ignacio and Schlegel,[28] Sakai and Nakamura,[29] and Becerra et al.[18] Ignacio and Schlegel have found two transition states (first order saddlepoints) and three second-order saddlepoints (two imaginary frequencies) all at the HF/6-31G(d) level. Sakai et al. have found two transition states and two minima at the MP2/6-311G-(d,p) level. They suggest that these two transition states must be passed through sequentially to proceed from $SiH_2 + SiH_4$

* Corresponding author. Phone: (+81)-3-5841-7295. Fax: (+81)-3-5841-7488. E-mail: matsumot@chemsys.t.u-tokyo.ac.jp.
† Department of Chemical System Engineering, The University of Tokyo.
‡ Sandia National Laboratories.
§ Environmental Science Center, The University of Tokyo.

10.1021/jp044121n CCC: $30.25
Published on Web 05/14/2005

to Si_2H_6. In contrast, Becerra et al. have found two minima and two transition states but suggest that the two transition states correlate with two alternative (parallel) paths from reactants to products. Recent ab initio calculations[22] provide a high level potential energy surface for the decomposition of Si_2H_6, and thus for each of the reactions of interest here. As part of the present analysis we will provide an improved description of the relevance of the various saddlepoints on the potential energy surface and provide further high level estimates for their energies.

These prior ab initio calculations clearly indicate that the saddlepoint energies for both reactions R1 and R2 are lower than the energies of the corresponding separated products. This finding implies significant errors when applying a fixed transition state RRKM model. The limitations in the use of a fixed transition state were commented on by Moffat et al.[16,17] in their nonlinear regression of RRKM calculations to experimental results. In particular, they noted that the use of a fixed transition state and weak collision efficiencies leads to uncertainties in the temperature extrapolation of the high-pressure rate constants. Becerra et al.[18] in their RRKM modeling of reactions R1 and R-1, concluded even more strongly that a fixed transition state for the $SiH_2 + SiH_4$ reaction is inadequate. Their more detailed exposition notes "that a transition state tightening effect occurs as the temperature increases between 300 and 660 K."

Smirnov[20] has performed RRKM calculations for reactions R1 and R2 including a treatment of the pressure dependence. He suggests that, because the energies of the saddlepoints on the potential energy surface are lower than the energies of the separate products, the transition state bottlenecks are located not at the saddlepoints but are moved toward the products for low energy collisions. At high energies the bottlenecks were postulated to be close to the energy maximum. He has avoided the ambiguities of fixed transition state models by using experimentally estimated Arrhenius preexponential factors and energy barriers for reactions R1 and R2 to generate sums of states for the transition states via inverse Laplace transforms. However, the lack of direct experimental data for reaction R2 makes this analysis somewhat unreliable.

Even though these limitations in a fixed transition state RRKM model have been noted, it has not yet been shown how to correctly derive the rate constants for complicated potential energy surfaces, in which reactants first form a weakly bonded adduct, and then pass over a saddlepoint whose energy is lower than that of the reactants. The prior RRKM analyses were also limited in the accuracy of the estimated transition state energies. One general conclusion of the prior RRKM modeling was that reaction R1 dominates over reaction R2. This result was primarily due to the lower heat of reaction for reaction R1. However, recent G3//B3LYP calculations indicated that the difference in the reaction enthalpies between reactions R1 and R2 is only 1.9 kcal/mol.[22] Thus, reaction R2 may become competitive with reaction R1 at high temperatures, particularly when the correct enthalpy of reaction and a proper treatment of the multiple transition states are incorporated. A reexamination of the branching ratios is certainly warranted.

Each of the reactions relevant to the thermal decomposition of disilane is, of course, pressure dependent. This pressure dependence has been examined in the prior RRKM calculations (see, e.g., refs 16−18). The study by Moffat et al.[16,17] indicated that under some conditions relating to thermal CVD of silicon, reaction R3 is important as a competitor with reaction R-1. Swihart et al.[27] have incorporated pressure dependent rate estimates for the Si_2H_6 system in their modeling of particle-growth during thermal CVD. They found that the total pressure has a large effect on the formation of silicon nanoparticles at low pressure, but little effect at atmospheric pressure. This finding was attributed to the pressure dependences of (R-1) and (R3).

In this paper, a novel two transition state model is employed to obtain a proper description of the thermal decomposition of disilane over a wide range of temperatures and pressures. In this two transition state model the "outer" or loose transition state is treated with phase space theory,[30−32] whereas the "inner" or tight transition state is treated as a fixed transition state (at the saddlepoint). The partition functions for the fixed inner transition states and for the Si_2H_6 complex are generally evaluated on the basis of rigid rotor harmonic oscillator assumptions but do employ one-dimensional hindered rotor treatments as necessary. The pressure dependences of the various reactions are studied with master equation simulations implementing the two transition state model for the microcanonical rate coefficients. Among other things, these simulations yield a clarification of the temperature and pressure dependences of the chemical activation reaction, (R3), and the stabilization reaction, (R-1).

2. Potential Energy Surface

The various stationary points on the Si_2H_6 potential energy surface have been determined with density functional theory employing the Becke-3 Lee−Yang−Parr functional[33] and the 6-311++G(d,p) basis set.[34] For reaction R1 we find three first order ("transition states") and two second-order saddlepoints. The structures for these saddlepoints and for the separated products are illustrated in Figure 1, and the corresponding geometrical parameters are listed in Table 1. Corresponding high level energy estimates are reported in Table 2. These high level estimates are obtained from G3//B3LYP[35] calculations[22] and from basis set extrapolation[36] of quadratic configuration interaction calculations with perturbative inclusion of the triples correction (QCISD(T))[37] employing the Dunning correlation consistent triple-ζ (cc-pvtz) and quadruple-ζ (cc-pvqz) basis sets.[38] The T1 diagnostics[39,40] for the QCISD(T) calculations, also reported in Table 2, are generally about 0.015 and thus do not suggest any major uncertainties in the QCISD(T) based energy estimates. The present transition state models for the inner transition state employ the basis set extrapolated QCISD-(T) energies.

Each of the first order saddlepoints have been previously determined at either the HF or MP2 levels of theory.[18,28,29] However, a complete description of their kinetic relevance is still lacking. Here, as appropriate and necessary, reaction path following calculations have been performed to verify the connections between the various saddlepoints. The geometry labels provided in Figure 1 correspond with those provided in ref 28.

In essence, structures B through E correlate with different torsional states of the same transition state. Structures B and E are both first-order saddlepoints (i.e., "transition states"), with structure E having the lowest energy. Structure C is a torsional maximum obtained by rotating the SiH_2 moiety in structure E by 180° relative to the SiH_4 moiety. Similarly structure D is a torsional maximum obtained by performing the same rotation from structure B. Alternatively, structure C is obtained by performing a relative rotation by 60° of the two SiH_3 moieties in structure B, whereas structure D is obtained by performing the same rotation in structure E. Note that structure A from ref 28 is absent here because, at the B3LYP/6-311++G(d,p) level, structure B is found to have C_s symmetry.

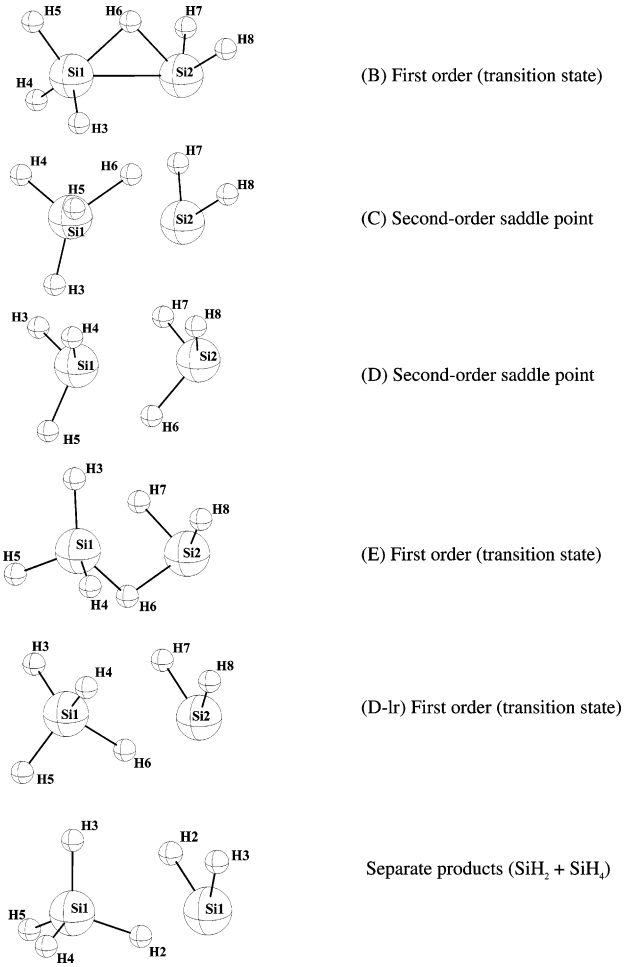

Figure 1. Transition state and second-order saddle point geometries for SiH_2 + SiH_4 at the B3LYP/6-311++G(d,p) level.

TABLE 1: Geometric Parameters of the Transition State and Second-Order Saddle Point for SiH_2 + SiH_4 Calculated at the B3LYP/6-311++G(d,p) Level[a]

structure in Figure 1	B	C	D	E	D-lr	SiH_4	SiH_2
symmetry	C_s	C_s	C_s	C_s	C_s	C_{3v}	C_{2v}
R(2−1)	2.455	2.675	2.649	2.739	2.996	1.484	1.527
R(3−1)	1.480	1.477	1.482	1.476	1.475	1.484	1.527
A(312)	99.73	93.15	107.50	98.72	98.63	109.47	91.50
R(4−1)	1.480	1.482	1.482	1.481	1.475	1.484	
A(412)	99.73	115.70	107.5	111.44	98.63	109.47	
D(4123)	242.62	246.90	240.72	243.77	244.85	240.00	
R(5−1)	1.492	1.482	1.486	1.482	1.482	1.484	
A(512)	129.40	115.70	115.55	115.22	124.41	109.47	
D(5123)	121.31	113.10	120.36	116.67	122.43	120.00	
R(6−2)	1.678	1.726	1.524	1.620	1.739		
A(621)	43.33	34.65	47.36	33.89	24.00		
D(6213)	238.69	180.02	239.64	185.96	237.58		
R(7−2)	1.501	1.513	1.495	1.520	1.522		
A(721)	108.99	100.99	74.84	71.13	74.44		
D(7213)	182.74	130.18	4.41	310.50	8.19		
R(8−2)	1.501	1.513	1.495	1.522	1.522		
A(821)	108.99	100.99	74.84	67.75	74.44		
D(8213)	294.64	229.82	114.86	55.32	106.97		

[a] Bond lengths are in angstroms; bond angles and dihedral angles are in degrees.

The treatment of these two torsional motions in the rate evaluations is complicated by the fact that the motion from structure E to structure B involves two coupled torsional motions. As a result, a coupled two-dimensional treatment is required for a completely accurate treatment. However, such a treatment is beyond the scope of this work. Instead, an approximate treatment involving a product of two uncoupled 1-dimensional hindered rotors for the $SiH_3\cdots SiH_3$ and $SiH_2\cdots SiH_4$ torsions is implemented here. This treatment reduces to the correct partition function at low temperature and at high temperature with only modest errors expected for intermediate temperatures.

TABLE 2: High Level Energy Estimates Obtained from G3//B3LYP Calculations and from Basis Set Extrapolation of QCISD(T)

	G3//B3LYP, kcal/mol	QCISD(T), kcal/mol	T1 diagnostics for QCISD(T)
SiH_2 + SiH_4 (separate products)	52.08	53.53	0.014 (SiH_2), 0.011 (SiH_4)
SiH_2 + SiH_4TS (B)	43.49	43.91	0.015
SiH_2 + SiH_4 second order (C)	46.73	48.17	0.015
SiH_2 + SiH_4 second order (D)	45.22	46.31	0.017
SiH_2 + SiH_4TS (E)	42.01	43.38	0.018
SiH_2 + SiH_4TS (D-lr)		45.23	0.016
H_3SiSiH + H_2 (separate products)	54.02	55.27	0.016 (H_3SiSiH), 0.006 (H_2)
H_3SiSiH + H_2 TS	51.03	51.86	0.013
Si_2H_6	0	0	0.013

The torsional potential employed for the $SiH_3\cdots SiH_3$ mode is designed to reproduce the difference in potential between configurations E and D and also the harmonic frequency of 71 cm^{-1} for the corresponding mode in configuration E. Meanwhile, the torsional potential for the $SiH_2\cdots SiH_4$ mode is assumed, incorrectly, to lead to configuration B. This incorrect assumption is introduced to obtain a torsional potential that has two minima and two maxima, over the range of torsions considered in geometries B through E. The parameters in the $SiH_2\cdots SiH_4$ torsional potential are designed to reproduce the difference in potential between configurations E and B and also the harmonic frequency of 326 cm^{-1} for the corresponding mode in configuration E. Again, these assumptions yield a torsional partition function that should be correct at low temperatures, because it reproduces the harmonic potential in the lowest energy state, and at high temperatures, because it has the correct restriction in torsional angles.

Sakai and Nakamura[29] have suggested that the process from reactants to products via structure E requires the sequential passage over two separate first-order saddlepoints. We have located those two saddlepoints and the corresponding two long-range complexes at the MP2/6-311G(d,p) level[41,42] as in ref 29. However, at the B3LYP/6-311++G(d,p) level it is not clear whether the second minimum and second saddlepoint exist. In particular, reaction path following from the first saddlepoint appears to lead to complex 2 (in Sakai and Nakamura's notation). However, attempts to optimize this geometry with tight convergence criteria led directly to the Si_2H_6 minimum. Similarly, attempts to locate the second saddlepoint were unsuccessful. Nevertheless, the potential is clearly quite flat from the region of the first saddlepoint in toward the Si_2H_6 complex and a variational treatment of the region between the two "apparent" saddlepoints would be valuable at some point. However, because such an analysis is likely to yield only modest corrections, due to the expected lower energy for the second saddlepoint, such an analysis is reserved for future work. Reaction path following from structure B, indicates that for this geometry there is no second minimum and saddlepoint, with the reaction path going smoothly and sharply down to the Si_2H_6.

Becerra et al.[18] have come to a somewhat different conclusion regarding the presence or absence of two sequential transition states. Their structure LM1 corresponds with complex 2 of Sakai and Nakamura, and the transition state TS1 corresponds with

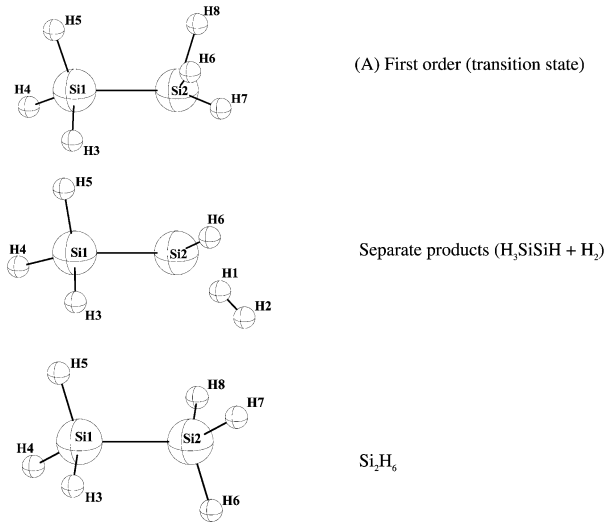

Figure 2. Transition state geometry for $H_3SiSiH + H_2$ at the B3LYP/6-311++G(d,p) level.

the second transition state of Sakai and Nakamura, the one that is absent in the present B3LYP analysis. In their effort to search for the other sequential transition state structure they considered a structure, LM2, which, unfortunately, is torsionally rotated from LM1. As a result, the transition state that they obtain from structure LM2 (TS2) in fact corresponds with the present structure B. They appear to have completely missed the present transition state E, which corresponds to the first of the sequential structures of Nakamura et al. As a result, they focus on their TS1, which is not the primary bottleneck for the path to Si_2H_6 for structures with the torsions of the present structure E.

Here, a second transition state structure corresponding to geometry D was found at the B3LYP level, with this structure having only one imaginary frequency. However, this second structure, labeled D-lr here, corresponds simply to a torsional rotation between two equivalent long-range complexes. These complexes are of the form of complex 1 of Sakai and Nakamura, but with the torsional angles of structure D. Thus, this transition state structure is essentially irrelevant to the kinetics. There may indeed be other such long-range torsional structures. We have not searched for them, because they should also be irrelevant to the kinetics.

At the B3LYP/6-311++G(d.p) level of theory, only one transition state is found for the channel leading to $H_3SiSiH + H_2$. The structures for the transition state and the separated products ($H_3SiSiH + H_2$) are illustrated in Figure 2, as are the structures for Si_2H_6. The corresponding geometrical parameters are listed in Table 3, and the high level energy estimates were also provided in Table 2. The rovibrational properties of the stationary points needed for the present transition state evaluations are summarized in Table 4, for both reactions R1 and R2. A one-dimensional hindered rotor treatment is incorporated for the relative motion of the SiH_3 and SiH groups in H_3SiSiH and for the $SiH_3\cdots SiH(H_2)$ motion at the saddlepoint.

The potential energy surface relevant to the thermal decomposition of disilane, as calculated at the extrapolated QCISD-(T) level of theory, is depicted in Figure 3. The density functional theory calculations described in this work have been performed with the GAUSSIAN 98 program suite[43] whereas the QCISD(T) calculations have been performed with MOLPRO.[44]

3. Derivation of Rate Constants

The thermal decomposition of disilane, where the saddlepoints leading to the product channels, $SiH_2 + SiH_4$ and $H_3SiSiH + H_2$, are lower in energy than the corresponding separated products, requires a two transition state treatment for each of the channels. An "inner" transition state precedes the formation of a long-range van der Waals complex and an "outer" transition state, at large separation between the product fragments, connects the long-range minimum to the product fragments, as indicated in Figure 3. These two transition states act in series and an approximate "dual" transition state model can be obtained under certain reasonable assumptions. In particular, if one assumes statistical probabilities for passing through each of these transition states upon each encounter, and further assumes that the flux between the two transition states is much greater than the flux at the transition states, then one arrives at an effective transition state sum of states given by[30,45,46]

$$\frac{1}{N_{TS}} = \frac{1}{N_{outer}} + \frac{1}{N_{inner}} \quad (1)$$

Here N_{TS} is the effective sum of states for the dual transition state model, N_{outer} is the sum of states for the outer transition state, and N_{inner} is the sum of states for the inner transition state located at the saddlepoint on the potential energy surface. For the $SiH_2 + SiH_4$ channel, the inner transition state is E in Figure 1 and the outer transition state corresponds to the van der Waals adduct decomposing to SiH_2 and SiH_4 without a reverse barrier. For the $H_3SiSiH + H_2$ channel, the inner transition state is structure A in Figure 2, and the outer transition state corresponds to its van der Waals adduct decomposing to $H_3SiSiH + H_2$ without a reverse barrier. For both channels, the outer transition state needs to be determined variationally.

In this study, phase space theory (PST)[30,31,32] is used to calculate N_{outer} and a direct count of the quantum rigid-rotor harmonic-oscillator rovibrational states for the saddlepoint is employed to calculate N_{inner} (but, with one or two of the modes treated as one-dimensional hindered rotors as discussed in the potential energy surfaces section). In PST the transition state involves two freely rotating fragments, whose vibrational modes are assumed to be identical to those of the fragments. The rotational modes are approximated as free rotations. An attractive fragment−fragment potential of the form R^{-n} is used, where n is usually 6 for neutral reactions, R is the separation between

TABLE 3: Geometric Parameters of the Transition State for $H_3SiSiH + H_2$ Calculated at the B3LYP/6-311++G(d,p) Level[a]

structure in Figure 2	TS	H_3SiSiH	H_2	Si_2H_6
symmetry	C_1	C_S	D_h	D_{3h}
R(2−1)	2.362	2.410	0.744	2.354
R(3−1)	1.487	1.493		1.487
A(312)	107.61	109.68		110.38
R(4−1)	1.487	1.488		1.487
A(412)	108.66	114.07		110.38
D(4123)	243.00	239.05		240.00
R(5−1)	1.486	1.493		1.487
A(512)	115.39	109.68		110.38
D(5123)	122.26	118.09		120.00
R(6−2)	1.653	1.527		1.487
A(621)	77.64	88.93		110.38
D(6213)	297.24	300.95		60.00
R(7−2)	1.550			1.487
A(721)	104.76			110.38
D(7213)	326.24			300.00
R(8−2)	1.496			1.487
A(821)	109.64			110.38
D(8213)	217.87			180.00

[a] Bond lengths are in angstroms, bond angles and dihedral angles in degrees.

TABLE 4: Parameters for the Rate Constant Calculations

	Si_2H_6	SiH_4	SiH_2	inner TS	H_3SiSiH	H_2	inner TS
frequency[a]/cm^{-1}	380	922	1025	98i	369	4418	1042i
	380	922	2042	512	388		337
	423	922	2042	632	428		409
	636	980		648	717		423
	636	980		890	868		582
	855	2234		913	932		692
	928	2242		954	956		815
	945	2242		959	2039		893
	945	2242		1020	2177		938
	959			1175	1286		973
	959			1742	2213		1016
	2209			2051			1698
	2218			2059			2044
	2218			2238			2170
	2218			2256			2211
	2228			2272			2217
	2228						2223
no. of hindred rotors	1	0	0	2	1	0	1
rotational constants/cm^{-1}	1.434	2.849	7.894	1.570	2.079	60.408	1.363
	0.1672	2.849	6.987	0.1386	0.1783	60.408	0.1716
	0.1672	2.849	3.706	0.1381	0.1741	0	0.168
rotational symmetry no.	18	12	2	3	3	2	1.5

[a] Vibrational frequencies calculated at the B3LYP/6-311++G(d,p) level. Imaginary frequencies are shown as i.

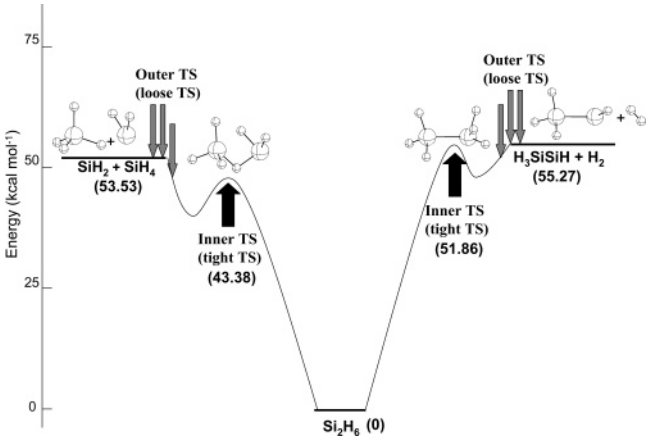

Figure 3. Potential energy surface relevant to the thermal decomposition of disilane, as calculated at the extrapolated QCISD(T) level.

the centers-of-mass of the two fragments, and C is a coefficient for the potential:

$$V = -\frac{C}{R^6} \tag{2}$$

Effective energy barriers are calculated as a function of the orbital angular momentum quantum number of the two fragments, l, and N_{outer} denotes the total number of these vibrational−rotational-orbital states that have a radial kinetic energy greater than that of the l-dependent effective barrier. The allowed l's must also be consistent with the triangular inequality in the total angular momentum, the total fragment angular momentum, and the orbital angular momentum. The position of the outer transition state, R^+, is defined by the position of the energy maximum on the effective potential (centrifugal + potential energy) surface. The R^+ varies with l, and there are a number of such $R^+(l)'$s for each given total angular momentum, J.

Here, for (R1), the value for the parameter C in eq 2 is determined from a fit to the high-pressure limiting rate constant for the reaction of SiH_2 with SiH_4, $k_{-1} + k_3$, near room temperature as derived by Becerra et al.[18] from RRKM calculations using a fixed transition state. The resulting value of C is 6.0×10^5 cm^{-1} $Å^6$ for reaction R1, which is in reasonable agreement with expectations from the literature.[47] For (R2), there are no good experimental data to fit, and we simply employ the same value for C. However, at least for 400 K and above, the predictions for (R2) are largely independent of the outer transition state treatment, and thus of the corresponding value chosen for C.

The rotational symmetry numbers employed for the reactant, products and transition states are reported in Table 4. The rotational symmetry numbers for the outer transition states were taken to be equal to the product of those for the corresponding bimolecular fragments. These symmetry numbers yield a reaction path degeneracy of 6 for the inner transition state in the dissociation to form $SiH_2 + SiH_4$ and a reaction path degeneracy of 8 for the reverse reaction. This degeneracy corresponds to the possible loss of any one of the 6 H atoms from the complex or alternatively, for the reverse addition reaction, to the attack of any one of the H atoms in SiH_4 by the SiH_2 group from two different possible orientations. The contributions from the different relative orientations of the two SiH_3 groups are incorporated with the hindered rotor treatments of the Si_2H_6 and of the inner transition state.

For the dissociation to form H_3SiSiH these symmetry numbers yield a reaction path degeneracy of 12, corresponding to the six different pairs of H_2 that can be lost and the two different orderings for each H_2 pair. For the reverse reaction these symmetry numbers yield a reaction path degeneracy of four, corresponding to the two different sides of attack and the two different orientations of H_2. Note that the symmetry number of 1.5 for the inner transition state arises from the product of 3 for the hindered rotor treatment of the $SiH_3\cdots SiH(H_2)$ mode, and a factor of $^1/_2$ arising from the presence of two enantiomers.

The micro canonical rate constant, $k(E,J)$, takes the standard RRKM form,

$$k(E,J) = \frac{N_{TS}(E,J)}{h\rho(E,J)} \tag{3}$$

where $\rho(E,J)$ is the density of states of the reactants, and h is Planck's constant. The density of states for the Si_2H_6 complex was obtained from rigid-rotor harmonic oscillator assumptions for all but the $SiH_3\cdots SiH_3$ torsional mode, for which a one-

dimensional hindered rotor treatment was employed. The microcanonical rate constant is averaged over a thermal equilibrium distribution function to obtain the canonical high-pressure limiting rate constant. To calculate the channel specific canonical rate constants at lower pressures, microcanonical rate constants for each channel are averaged over the nonequilibrium distribution functions. One-dimensional master equations for the multichannel dissociation of Si_2H_6 or the multichannel chemical activation reactions (reactions R-1 and R3) were solved to derive the nonequilibrium distribution functions for each channel.

An exponential down energy transfer model and Lennard Jones collision rates were employed in the master equation simulations. The average energy transferred in downward collisions $\langle \Delta E_{down} \rangle$ was assumed to be equal to 150 $(T/298)^{0.85}$ cm^{-1}, where T is in K. This form is representative of typical results in related studies[48−50] and is found to satisfactorily reproduce the experimental observations for the pressure dependence of the reaction of SiH_2 with SiH_4. The parameters for the Lennard-Jones collision rates were obtained from the CHEMKIN transport database and are given by $\sigma = 4.83$, 4.08, and 3.33 Å and by $\epsilon = 210$, 144, and 95 cm^{-1} for Si_2H_6, SiH_4, and Ar, respectively.

In the present study, all the rate constant calculations were performed with the VARIFLEX program suite developed by Klippenstein and co-workers.[51−55] VARIFLEX is a program package for the calculations of the rate constants for multichannel, muti-well reactions on the basis of variable reaction coordinate transition state theory (VRC-TST). Here, N_{outer} is calculated according to quantum phase space theory with a constant integration step size of 1 for the angular momentum variables. N_{inner} is evaluated via a direct count of quantum states at the inner fixed transition state. Both of these evaluations are performed at the energy, E, and total angular momentum, J, resolved level. Channel specific thermal rate constants for the $SiH_2 + SiH_4$ reactions (k_{-1} and k_3) were calculated by solving the multichannel master equations. Rate constants for the dissociation channels (k_1 and k_2) were evaluated at the same time. Rate constants for the chemical activation reactions $H_3SiSiH + H_2$ (k_{-2} and k_{-3}) may be obtained from those for the reverse reaction multiplied by the relevant equilibrium constants. The parameters required for the rate constant calculations in VARIFLEX are summarized in Tables 2 and 4.

4. Results and Discussion

We have considered two separate transition state models in the calculations of the rate constants. In the "fixed transition state" model (F-TST), only the inner transition state is taken into account; i.e., N_{TS} is equated with N_{inner}. The previous RRKM calculations of Si_2H_6 dissociation[14−21] were largely based on this F-TST model with semiempirical determinations of the transition states parameters. In the present study, parameters for the transition states (vibrational frequencies, moments of inertia, energy barrier height) are taken directly from the quantum chemical calculations, as listed in Tables 2 and 4. The other transition state model, termed the "dual transition state" model (D-TST) here, was described in the previous section. Briefly, in this model, two transition states, an inner and an outer, are considered and N_{TS} is evaluated from eq 1.

It is interesting to begin with a comparison of the predictions obtained from the F-TST, D-TST, and PST models for the high-pressure limiting rate coefficients. The predictions from these three models are plotted versus temperature in Figures 4 and 5, for reactions R-1 and R-2, respectively. Interestingly, for reaction R-1 the D-TST model is seen to differ significantly from both

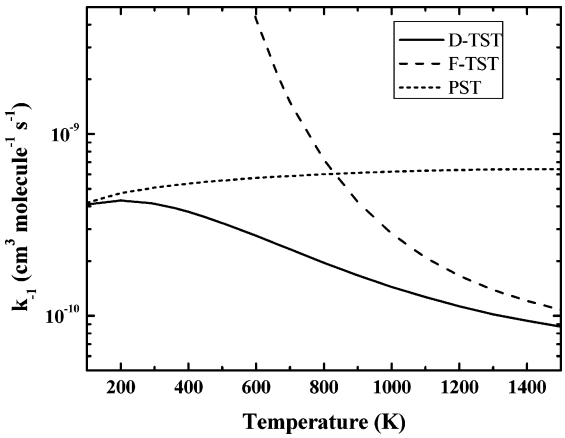

Figure 4. Plots of the temperature dependences of the D-TST, F-TST, and PST theoretical predictions for the $SiH_4 + SiH_2$ high-pressure limit rate coefficient.

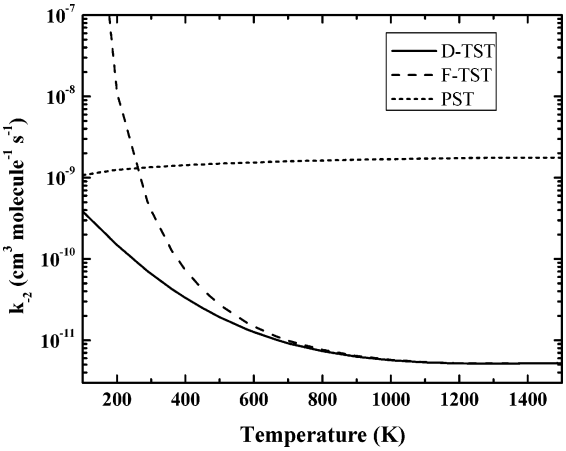

Figure 5. Plots of the temperature dependences of the D-TST, F-TST, and PST theoretical predictions for the $H_3SiSiH + H_2$ high-pressure limit rate coefficient.

the F-TST and PST models throughout the important temperature range from 300 to 1500 K. Clearly, neither the inner or outer transition state models can adequately describe the kinetics of the $SiH_2 + SiH_4$ addition reaction for temperatures of importance to CVD. In contrast, the F-TST model alone provides an adequate description of the kinetics of the $H_3SiSiH + H_2$ reaction for the key CVD temperature range 700−1500 K. Thus, in our predictions for the pressure dependent rate coefficients described below, we consider both the D-TST and F-TST models for reaction R1, but only the F-TST model for reaction R2.

4.1. Dissociation of Si_2H_6. The present predictions for the high-pressure limiting rate constants for reaction R1 are depicted in Figure 6. Again, at low temperatures the rate constant calculated with the F-TST model is considerably larger than that derived from the D-TST model. As temperature increases the difference becomes smaller, and above 1500 K, the rate constants calculated by the two models are in reasonably good agreement with each other. This finding indicates that the outer transition state provides the rate-limiting bottleneck at low temperatures, whereas the inner transition state becomes the dominant bottleneck at high temperatures. In other words, N_{TS} is mainly determined by N_{outer} at low temperatures whereas N_{TS} is almost equal to N_{inner} at high temperatures. This variation in the dominance of the two transition states is caused by the difference in the density of states at the inner and the outer transition states. The outer transition state is loose, with a high

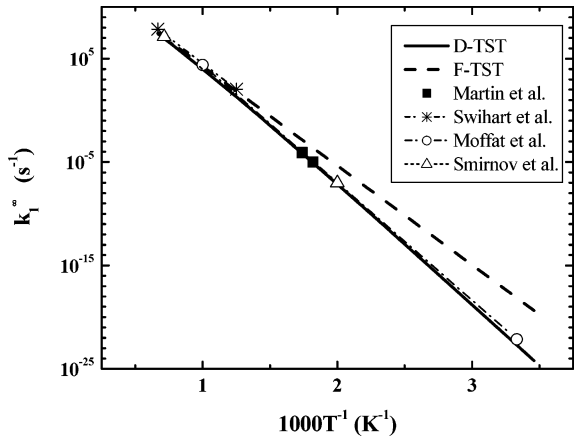

Figure 6. Plots of the high-pressure limit rate constant for (R1), k_1, versus the inverse of temperature. The solid line denotes k_1 calculated in this study with the dual transition state model for reaction R1 and the fixed transition state model for reaction R2; the broken line denotes k_1 calculated in this study with the fixed transition state model for both reactions R1 and R2; ○ and the dashed line denote k_1 calculated by Moffat et al.;[16,17] △ and the dashed line denote k_1 calculated by Smirnov et al.;[20] ∗ and the dashed line denote k_1 calculated by Swihart et al.;[21] ■ denotes experimental results from Martin et al. in C_3H_8 at the high-pressure limit.[9]

entropy, whereas the inner transition state is tight, with a low entropy. As a result, the density of states at the outer transition state is much higher than that at the inner transition state. When the available energy is high enough, N_{outer} is then much greater than N_{inner}, and N_{TS} is equal to N_{inner}. On the other hand, when the available energy, E, is close to the product states, the number of states at the transition state is larger for the inner transition state because of larger available energy (i.e., $(E - E_{0,inner}) > (E - E_{0,outer})$).

In Figure 6, literature values of k_1^∞ are also compared with the present predictions. Both the values of Moffat et al.[17] and Smirnov[20] were calculated with F-TST parameters adjusted to give agreement with the experimental values of Martin et al.[9] On the other hand, the most recent evaluation of the rate constant by Swihart and Carr[21] used F-TST parameters obtained from quantum chemical calculations. Their result in the high-temperature region is in good agreement with the present F-TST rate constant. At lower temperatures, the D-TST rate constant is also in good agreement with the experimental estimate of Martin et al. This improved agreement indicates the validity of the D-TST treatment for reaction R1.

For reaction R2, in contrast with reaction R1, the rate constants derived from the F-TST and D-TST models were essentially identical above 600 K. This finding indicates that passage through the inner transition state is the rate determining step for reaction R2; at least for temperatures of 600 K and higher. For this channel, the difference between the energy of the inner transition state and the product state is relatively small (−3.4 kcal/mol). As a result, the number of states at the inner transition state is much lower than that at the outer transition state, except at quite low energies. In this case, the thermal rate constant reduces to that obtained from the F-TST model at a much lower temperature, i.e., about 600 K, and the F-TST treatment is valid for the temperatures of interest here.

The pressure dependences of the rate constants k_1 and k_2 are shown in Figure 7a,b, respectively. Values for k_1 derived from the F-TST treatment (dash lines) and from the D-TST treatment (solid lines) (for (R1)) are compared in Figure 7a. The F-TST model predicts larger rate constants, with the greatest difference

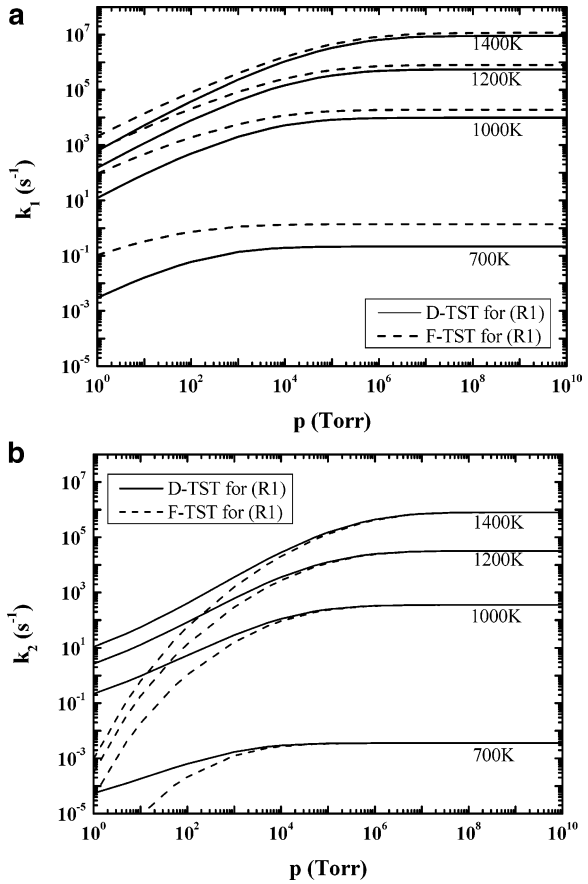

Figure 7. (a) Plots of the pressure dependence of the calculated rate constant, k_1 in silane buffer. The solid line denotes the results obtained with the dual transition state model for reaction R1 and the fixed transition state model for reaction R2; the broken line denotes the results obtained with the fixed transition state model for both reactions R1 and R2. The temperatures considered here are as follows: 1, 700 K; 2, 1000 K; 3, 1200 K; 4, 1400 K. (b) Plots of the pressure dependence of the calculated rate constant, k_2 in silane buffer. The solid line denotes the results obtained with the dual transition state model for reaction R1 and the fixed transition state model for reaction R2; the broken line denotes the results obtained with the fixed transition state model for both reactions R1 and R2. The temperatures considered here are as follows: 1, 700 K; 2, 1000 K; 3, 1200 K; 4, 1400 K.

at lower pressures. This increasing difference between the F-TST and D-TST models with decreasing pressure at first seems counterintuitive given the fact that the rate coefficient should become independent of the transition state flux in the low pressure limit. However, the use of a negative energy relative to products in the F-TST models effectively lowers the dissociation threshold. This lowering of the dissociation threshold is what results in the increase in its predictions for the low-pressure limit rate constants.

The rate constants for reaction R2 are plotted in Figure 7b. These rate constants are calculated with the F-TST model for reaction R2 and with both the F-TST (dash lines) and D-TST (solid lines) models for reaction R1. Interestingly, at low pressures the rate constant for reaction R2 is affected by the transition state model employed for reaction R1. This dependence arises from the coupling of reactions R1 and R2 in the multichannel master equation, with the nonequilibrium distribution function being greatly affected by the particular transition state model employed for reaction R1. When the F-TST model is used for reaction R1, the low energy flux to reaction R1 is overestimated, and the rate constant for reaction R2 is underestimated at low pressures, as can be seen in this figure.

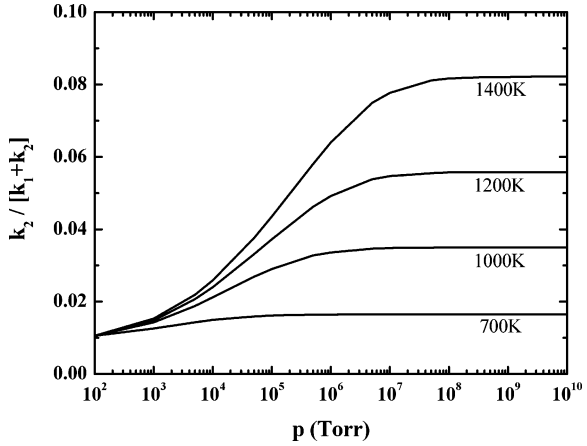

Figure 8. Plots of the pressure dependence of the predicted branching ratio for (R1) and (R2). The temperatures considered here are as follows: 1, 700 K; 2, 1000 K; 3, 1200 K; 4, 1400 K.

The contribution of reaction R2 to the thermal dissociation of Si_2H_6 is very important in silicon CVD processes. The calculated branching fraction, $k_2/(k_1 + k_2)$, is plotted in Figure 8 as a function of pressure for a number of temperatures. As expected, the branching fraction for (R2) increases with increasing temperature and with increasing pressure. At a temperature of 1400 K the branching fraction is equal to 0.08 in the high-pressure limit. However, reaction R2 is negligible at pressures below 100 Torr, as shown in Figure 8.

The calculated high-pressure limit rate constants in the 300−1500 K temperature range are well described by the Arrhenius forms $10^{15.24}$ exp(−25940/T) s^{-1} and $10^{14.17}$ exp(−26740/T) s^{-1} for (R1) and for (R2), respectively.

4.2. $SiH_2 + SiH_4$ Reaction. The chemical activation reaction of $SiH_2 + SiH_4$ has two channels, reactions R-1 and R3. The calculations of the rate constant for reaction R3 require transition states for (R1) and (R2). Although the rate constant for reaction R-1 can be derived from the rate constant for reaction R1 via the equilibrium constant, microcanonical rate constants for reaction R1 are also needed to solve the master equation for reaction R3. Therefore the rate constants for reactions R-1 and R3 are calculated at the same time in the VARIFLEX program. The D-TST model is applied to (R1) and the F-TST model is used for (R2), as before.

The rate constant for the overall decay of SiH_2 in the reaction of SiH_2 with SiH_4, $k_{-1} + k_3$, is compared in Figure 9 with the experimental results of Becerra et al.[18] These results are for reaction in the presence of Ar buffer gas. The overall agreement is quite satisfactory, with the pressure dependence in the falloff region being well reproduced. The negative temperature dependence of the overall decay rate is caused by the negative temperature dependence of k_{-1}.

The pressure dependences of the rate constants in SiH_4 buffer gas are depicted in Figure 10a for reaction R-1 and in Figure 10b for reaction R3. As shown in these figures, reaction R-1 has a negative temperature dependence, whereas reaction R3 has a positive dependence. The pressure dependence of reaction R3 is typical of chemical activation reactions. The rate constant for reaction R3 goes to zero in the high-pressure limit. In the high-pressure region, reaction R-1 is the main channel for the $SiH_2 + SiH_4$ reaction. However, at low pressures and at high temperatures, reaction R3 becomes important. The branching fraction of $k_3/(k_{-1} + k_3)$ is depicted in Figure 11 for several temperatures. At pressures below 100 Torr and at temperatures

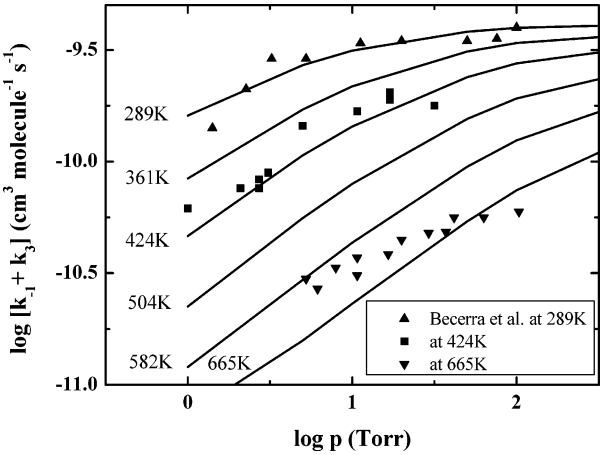

Figure 9. Plots of the pressure dependence of the rate constant, $k_{-1} + k_3$ in argon buffer. The temperatures considered here are as follows: 1, 289 K; 2, 361 K; 3, 424 K; 4, 504 K; 5, 582 K; 6, 665 K. ▲ denotes experimental results by Becerra et al. at 289 K, ■ at 424 K, and ▼ at 665 K.[18]

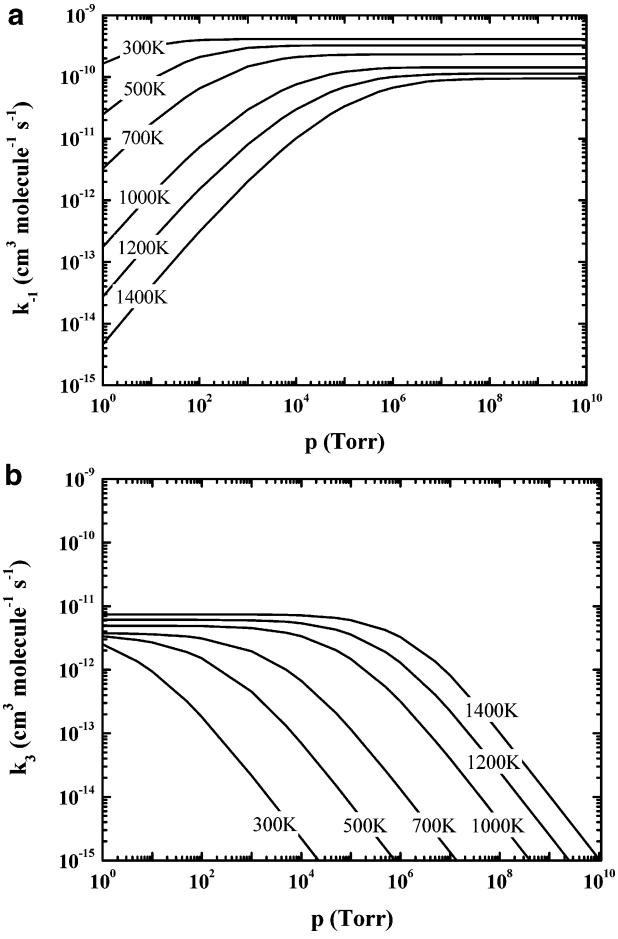

Figure 10. (a) Plots of the pressure dependence of the calculated rate constant, k_{-1} in silane buffer. The temperatures considered here are as follows: 1, 300 K; 2, 500 K; 3, 700 K; 4, 1000 K; 5, 1200 K; 6, 1400 K. (b) Plots of the pressure dependence of the calculated rate constant, k_3 in silane buffer. The temperatures considered here are as follows: 1, 300 K; 2, 500 K; 3, 700 K; 4, 1000 K; 5, 1200 K; 6, 1400 K.

higher than 1100 K, reaction R3 is the dominant channel in the $SiH_2 + SiH_4$ reaction. This finding will greatly affect simulations of the thermal CVD processes of silicon.

The calculated rate constants in the 300−1500 K temperature range are roughly described by the Arrhenius forms $10^{-10.08}$ exp (575.7/T) cm^3 $molecule^{-1}$ s^{-1} for k_{-1} in the high-pressure

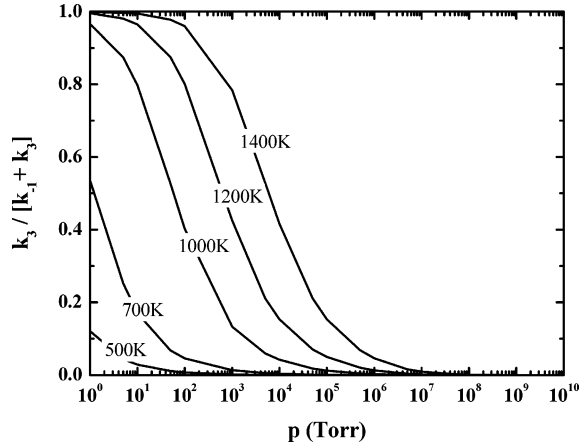

Figure 11. Plots of the pressure dependence of the branching ratio for (R-1) and (R3). The temperatures considered here are as follows: 1, 500 K; 2, 700 K; 3, 1000 K; 4, 1200 K; 5, 1400 K.

limit and $10^{-11.12}$ exp $(-370.3/T)$ cm^3 molecule^{-1} s^{-1} for k_3 in the low-pressure limit, respectively.

5. Conclusions

Rate constants relevant to the thermal dissociation of Si_2H_6 have been calculated for the various multichannel unimolecular dissociations and chemical activation reactions. Quantum chemical calculations indicate that the energies of the saddlepoints for reactions R1 and R2 are lower than the energies of the product states. A dual transition state model was applied to reaction R1. It is found that reaction R2 is well described by a fixed transition state model, at least for 600 K and higher, whereas a dual transition state treatment is required for reaction R1 for all temperatures considered here (300−1500 K). The calculated high-pressure limit rate constant for reaction R1 is in good agreement with the previous experimental and theoretical estimations. It is confirmed that the contribution of reaction R2 is negligible under the usual thermal CVD conditions. The rate constants for the chemical activation reaction of SiH_2 + SiH_4 are also evaluated. At low temperatures, reaction R-1 is the main channel for the pressures relevant to silicon thermal CVD processes. However, the contribution of reaction R3 becomes larger, and even dominant, at higher temperatures and at lower pressures.

Acknowledgment. The work at Sandia is supported by the Division of Chemical Sciences, Geosciences, and Biosciences, the Office of Basic Energy Sciences, the U.S. Department of Energy. Sandia is a multiprogram laboratory operated by Sandia Corporation, a Lockheed Martin Company, for the National Nuclear Security Administration under contract DE-AC04-94-AL85000.

References and Notes

(1) Jasinski, J. M.; Gates, S. M. *Acc. Chem. Res.* **1991**, *24*, 9.
(2) Breiland, W. G.; Coltrin, M. E. *J. Electrochem. Soc.* **1990**, *137*, 2313.
(3) Ho, P.; Coltrin, M. E.; Breiland, W. G. *J. Phys. Chem.* **1994**, *98*, 10138.
(4) Jasinski, J. M.; Becerra, R.; Walsh, R. *Chem. Rev.* **1995**, *95*, 1203.
(5) Becerra, R.; Walsh, R. In *Research in Chemical Kinetics III*; Compton, G., Walsh, R., Eds.; Elsevier: Amsterdam, 1996; p 263.
(6) Tonokura, K.; Koshi, M. *Curr. Opin. Solid State Mater. Sci.* **2002**, *6*, 479.
(7) Bowrey, M.; Purnell, J. H. *Proc. R. Soc. London A.* **1971**, *321*, 341.
(8) Olbrich, G.; Potzinger, P.; Reimann, B.; Walsh, R. *Organometallics* **1984**, *3*, 1267.
(9) Martin, J. G.; Ring, M. A.; O'Neal, H. E. *Int. J. Chem. Kinet.* **1987**, *19*, 715.
(10) Martin, J. G.; O'Neal, H. E.; Ring, M. A. *Int. J. Chem. Kinet.* **1990**, *22*, 613.
(11) Han, J. H.; Rhee, S.; Moon, S. H. *J. Electrochem. Soc.* **1996**, *143*, 1996.
(12) Dzarnoski, J.; Rickborn, S. F.; O'Neal, H. E.; Ring, M. A. *Organometallics* **1982**, *1*, 1217.
(13) Mick, H. J.; Markus, M. W.; Roth, P.; Smirnov, V. N. *Ber. Bunsen-Ges. Phys. Chem.* **1995**, *99*, 880.
(14) Frey, H. M.; Walsh, R.; Watts, I. M. *J. Chem. Soc., Chem. Commun.* **1986**, 1189.
(15) (a) Roenigk, K. F.; Jensen, K. F.; Carr, R. W. *J. Phys. Chem.* **1987**, *91*, 5732. (b) Roenigk, K. F.; Jensen, K. F.; Carr, R. W. *J. Phys. Chem.* **1988**, *92*, 4254.
(16) Moffat, H. K.; Jensen, K. F.; Carr, R. W. *J. Phys. Chem.* **1992**, *96*, 7683.
(17) Moffat, H. K.; Jensen, K. F.; Carr, R. W. *J. Phys. Chem.* **1992**, *96*, 7696.
(18) Becerra, R.; Frey, H. M.; Mason, B. P.; Walsh, R.; Gordon, M. S. *J. Chem. Soc., Faraday Trans.* **1995**, *91*, 2723.
(19) Mick, H. J.; Roth, P.; Sminrov, V. N. *Kinet. Catal.* **1996**, *37*, 5.
(20) Smirnov, V. N. *Kinet. Catal.* **1997**, *38*, 339.
(21) Swihart, M. T.; Carr, R. W. *J. Phys. Chem. A* **1998**, *102*, 1542.
(22) Tonokura, K.; Murasaki, T.; Koshi, M. *J. Phys. Chem. B* **2002**, *106*, 555.
(23) Inoue, G.; Suzuki, M. *Chem. Phys. Lett.* **1985**, *122*, 361.
(24) Jasinski, J. M.; Chu, J. O. *J. Chem. Phys.* **1988**, *88*, 1678.
(25) Baggott, J. E.; Frey, H. M.; Lightfoot, P. D.; Walsh, R.; Watts, I. M. *J. Chem. Soc., Faraday Trans.* **1990**, *86*, 27.
(26) Becerra, R.; Frey, H. M.; Mason, B. P.; Walsh, R.; Gordon, M. S. *J. Am. Chem. Soc.* **1992**, *114*, 2751.
(27) Girshick, S. L.; Swihart, M. T.; Suh, S. M.; Mahajan, M. R.; Nijhawan, S. *J. Electrochem. Soc.* **2000**, *147*, 2303.
(28) Ignacio, E. W.; Schlegel, H. B. *J. Phys. Chem.* **1992**, *96*, 1758.
(29) Sakai, S.; Nakamura, M. *J. Phys. Chem.* **1993**, *97*, 4960.
(30) Klippenstein, S. J.; Khundkar, L. R.; Zewail, A. H.; Marcus, R. A. *J. Chem. Phys.* **1988**, *89*, 4761.
(31) Pechukas, P.; Light, J. C. *J. Chem. Phys.* **1965**, *42*, 3281. Light, J. C.; Lin, J. *J. Chem. Phys.* **1965**, *43*, 3209. Pechukas, P.; Rankin, R.; Light, J. C. *J. Chem. Phys.* **1966**, *44*, 794.
(32) Nikitin, E. E. *Teor. Eksp. Khim. Acad. Nauk. Ukr. SSR* **1965**, *1*, 428.
(33) Becke, A. D. *J. Chem. Phys.* **1993**, *98*, 5648.
(34) Hehre, W. J.; Radom, L.; Pople. J. A.; Schleyer, P. v. R. *Ab Initio Molecular Orbital Theory*; Wiley: New York, 1987.
(35) Baboul, A. G.; Curtiss, L. A.; Redfern, P. C.; Rassolov, V. J. *J. Chem. Phys.* **1999**, *110*, 7650.
(36) Miller, J. A.; Klippenstein, S. J. *Phys. Chem. Chem. Phys.* **2004**, *6*, 1192.
(37) Pople, J. A.; Head-Gordon, M.; Raghavachari, K. *J. Chem. Phys.* **1987**, *87*, 5968.
(38) Dunning, T. H. *J. Chem. Phys.* **1989**, *90*, 1007.
(39) Lee, T. J.; Taylor, P. R. *Int. J. Quantum Chem. Symp.* **1989**, *23*, 199.
(40) Lee, T. J.; Rendell, A. P.; Taylor, P. R. *J. Phys. Chem.* **1990**, *94*, 5463.
(41) Head-Gordon, M.; Pople, J. A.; Frisch, M. J. *Chem. Phys. Lett.* **1988**, *153*, 503.
(42) Moller, C.; Plesset, M. C. *Phys. Rev.* **1934**, *46*, 618.
(43) Frisch, M. J.; Trucks, G. W.; Schlegel, H. B.; Scuseria, G. E.; Robb, M. A.; Cheeseman, J. R.; Montgomery, J. A., Jr.; Vreven, T.; Kudin, K. N.; Burant, J. C.; Millam, J. M.; Iyengar, S. S.; Tomasi, J.; Barone, V.; Mennucci, B.; Cossi, M.; Scalmani, G.; Rega, N.; Petersson, G. A.; Nakatsuji, H.; Hada, M.; Ehara, M.; Toyota, K.; Fukuda, R.; Hasegawa, J.; Ishida, M.; Nakajima, T.; Honda, Y.; Kitao, O.; Nakai, H.; Klene, M.; Li, X.; Knox, J. E.; Hratchian, H. P.; Cross, J. B.; Adamo, C.; Jaramillo, J.; Gomperts, R.; Stratmann, R. E.; Yazyev, O.; Austin, A. J.; Cammi, R.; Pomelli, C.; Ochterski, J. W.; Ayala, P. Y.; Morokuma, K.; Voth, G. A.; Salvador, P.; Dannenberg, J. J.; Zakrzewski, V. G.; Dapprich, S.; Daniels, A. D.; Strain, M. C.; Farkas, O.; Malick, D. K.; Rabuck, A. D.; Raghavachari, K.; Foresman, J. B.; Ortiz, J. V.; Cui, Q.; Baboul, A. G.; Clifford, S.; Cioslowski, J.; Stefanov, B. B.; Liu, G.; Liashenko, A.; Piskorz, P.; Komaromi, I.; Martin, R. L.; Fox, D. J.; Keith, T.; Al-Laham, M. A.; Peng, C. Y.; Nanayakkara, A.; Challacombe, M.; Gill, P. M. W.; Johnson, B.; Chen, W.; Wong, M. W.; Gonzalez, C.; Pople, J. A. *Gaussian 98*, Revision A11; Gaussian, Inc.: Pittsburgh, PA, 2003.
(44) MOLPRO, version 2002.1, is a package of ab initio programs written by Werner, H.-J.; Knowles, P. J. with contributions from Amos, R. D.; Bernhardsson, A.; Berning, A.; Celani, P.; Cooper, D. L.; Deegan, M. J. O.; Dobbyn, A. J.; Eckert, F.; Hampel, C.; Hetzer, G.; Korona, T.; Lindh, R.; Lloyd, A. W.; McNicholas, S. J.; Manby, F. R.; Meyer, W.; Mura, M.

E.; Nicklaâ, A.; Palmieri, P.; Pitzer, R.; Rauhut, G.; Schutz, M.; Schumann, U.; Stoll, H.; Stone, A. J.; Tarroni, R.; Thorsteinsson, T.; Werner, H.-J.
(45) Miller, W. H. *J. Chem. Phys.* **1976**, *65*, 2216.
(46) Rai, S. N.; Truhlar, D. G. *J. Chem. Phys.* **1983**, *79*, 6046.
(47) Berry, R. S.; Rice, S. A.; Ross, J. *Physical Chemistry*; Wiley: New York, 1980; p 413.
(48) Miller, J. A.; Klippenstein, S. J.; Raffy, C. *J. Phys. Chem. A* **2002**, *106*, 4904.
(49) Miller, J. A.; Klippenstein, S. J. *J. Phys. Chem. A* **2003**, *107*, 2687.
(50) Knyazev, V. D.; Slagle, I. R. *J. Phys. Chem.* **1996**, *100*, 16899.
(51) Klippenstein, S. J.; Wagner, A. F.; Dunbar, R. C.; Wardlaw, D. M.; Robertson, S. H.; Miller, J. A. VARIFLEX Version 1.13m, 2003.
(52) Klippenstein, S. J.; Miller, J. A. *J. Phys. Chem. A* **2002**, *106*, 9267.
(53) Klippenstein, S. J. *Chem. Phys. Lett.* **1990**, *170*, 71.
(54) Klippenstein, S. J. *J. Chem. Phys.* **1991**, *94*, 6469.
(55) Klippenstein, S. J. *J. Chem. Phys.* **1992**, *96*, 367.